J. Fluid Mech. (2014), *vol.* 741, *pp* 1–27.
doi:10.1017/jfm.2013.664

Sidewall effects in Rayleigh–Bénard convection

Richard J. A. M. Stevens[1,2], Detlef Lohse[1] and Roberto Verzicco[1,3,†]

[1]Department of Science and Technology and J.M. Burgers Center for Fluid Dynamics, University of Twente, PO Box 217, 7500 AE Enschede, The Netherlands

[2]Department of Mechanical Engineering, Johns Hopkins University, Baltimore, MD 21218, USA

[3]Department of Industrial Engineering, Università di Roma 'Tor Vergata', Via del Politecnico 1, 00133, Roma

(Received 1 July 2013; revised 10 December 2013; accepted 11 December 2013; first published online 17 February 2014)

We investigate the influence of the temperature boundary conditions at the sidewall on the heat transport in Rayleigh–Bénard (RB) convection using direct numerical simulations. For relatively low Rayleigh numbers Ra the heat transport is higher when the sidewall is isothermal, kept at a temperature $T_c + \Delta/2$ (where Δ is the temperature difference between the horizontal plates and T_c the temperature of the cold plate), than when the sidewall is adiabatic. The reason is that in the former case part of the heat current avoids the thermal resistance of the fluid layer by escaping through the sidewall that acts as a short-circuit. For higher Ra the bulk becomes more isothermal and this reduces the heat current through the sidewall. Therefore the heat flux in a cell with an isothermal sidewall converges to the value obtained with an adiabatic sidewall for high enough Ra ($\simeq 10^{10}$). However, when the sidewall temperature deviates from $T_c + \Delta/2$ the heat transport at the bottom and top plates is different from the value obtained using an adiabatic sidewall. In this case the difference does not decrease with increasing Ra thus indicating that the ambient temperature of the experimental apparatus can influence the heat transfer. A similar behaviour is observed when only a very small sidewall region close to the horizontal plates is kept isothermal, while the rest of the sidewall is adiabatic. The reason is that in the region closest to the horizontal plates the temperature difference between the fluid and the sidewall is highest. This suggests that one should be careful with the placement of thermal shields outside the fluid sample to minimize spurious heat currents. When the physical sidewall properties (thickness, thermal conductivity and heat capacity) are considered the problem becomes one of conjugate heat transfer and different behaviours are possible depending on the sidewall properties and the temperature boundary condition on the 'dry' side. The problem becomes even more complicated when the sidewall is shielded with additional insulation or temperature-controlled surfaces; some particular examples are illustrated and discussed. It has been observed that the sidewall temperature dynamics not only affects the heat transfer but can also trigger a different mean flow state or change the temperature fluctuations in the flow and this could explain some of the observed differences between similar but not fully identical experiments.

Key words: Bénard convection, convection

†Email address for correspondence: verzicco@uniroma2.it

1. Introduction

The classical system to study turbulent heat transfer is Rayleigh–Bénard (RB) convection, i.e. the motion of a fluid layer in a box heated from below and cooled from above (Ahlers, Grossmann & Lohse 2009*c*). The system has many applications in atmospheric and environmental physics, astrophysics and process technology. The control parameters of the system are the Rayleigh number $Ra = \beta g \Delta L^3/(\kappa\nu)$, the Prandtl number $Pr = \nu/\kappa$ and the aspect ratio $\Gamma = D/L$. Here, L and D are the height and diameter of the fluid sample, g the gravitational acceleration, Δ the temperature difference between the bottom and the top of the sample and β, ν and κ the thermal expansion coefficient, the kinematic viscosity and the thermal diffusivity of the fluid, respectively. Nowadays most experimental and numerical results on the Nusselt number Nu, the dimensionless heat transfer, agree up to $Ra \approx 2 \times 10^{11}$ and are in agreement with the description of the Grossmann–Lohse model (Grossmann & Lohse 2000, 2001, 2002, 2004; Stevens, van der Poel & Lohse 2013). However, for higher Ra the situation is more complex.

Most high-Ra experiments are performed in samples with aspect ratio $\Gamma = 1/2$ or smaller (for example $\Gamma = 0.23$ in Roche *et al.* 2010) owing to the dependence of Ra on L^3 that, for a given volume of fluid, favours the increase of L at the expense of D. Many of these experiments are performed with gaseous helium near its critical point (Castaing *et al.* 1989; Niemela *et al.* 2000, 2001; Chavanne *et al.* 2001; Roche *et al.* 2001*a*, 2002, 2010; Niemela & Sreenivasan 2006; Urban, Musilová & Skrbek 2011; Urban *et al.* 2012), and recently Funfschilling, Bodenschatz & Ahlers (2009), Ahlers *et al.* (2009*a*), Ahlers, Funfschilling & Bodenschatz (2009*b*, 2011) and He *et al.* (2012) performed measurements at room temperature using highly pressurized gases. As is shown in figure 1 there are significant deviations among all experiments for $Ra \gtrsim 2 \times 10^{11}$ and unfortunately there is no clear explanation for this disagreement.

The studies of Johnston & Doering (2009) and Stevens *et al.* (2011) showed that the differences among the experiments cannot be explained by the fact that some setups use a constant heat flux condition at the bottom plate instead of a constant temperature condition, nor by the variations of Pr (Stevens *et al.* 2011). Recently, evidence has been found that suggests that part of the deviation might be related to the formation of different turbulent states in the high-Ra regime. Multiple states in RB convection were observed by Roche *et al.* (2002), who found a bimodality of Nu with 7 % difference between the two data sets. Subsequently, Chillà *et al.* (2004) and Sun, Xi & Xia (2005*b*) showed that a finite tilt of the sample can cause a transition between different flow states. Later Xi & Xia (2008) and Weiss & Ahlers (2011) found that in a $\Gamma = 1/2$ sample the flow can be either in a single-roll state or in a double-roll state, each with a specific heat transport. Recently, Niemela & Sreenivasan (2010) found two $Nu/Ra^{1/3}$ branches in a $\Gamma = 1$ sample. The high-Ra branch is 20 % higher than the low-Ra branch. More recently, Ahlers and coworkers (see Funfschilling *et al.* 2009; Ahlers *et al.* 2009*a*,*b*, 2011; He *et al.* 2012) found two different branches in one experiment. In these experiments the difference between the average temperature inside the cell and the temperature outside the cell determines the state of the system. Also, in the experiments of Roche *et al.* (2010) two different turbulent states were observed in a $\Gamma = 0.23$ sample in the range $10^{12} \leqslant Ra \leqslant 10^{13}$. In addition, they showed that in the high-Ra regime the heat transport can very strongly depend on the characteristics of the sidewall and the aspect ratio. Finally, van der Poel, Stevens & Lohse (2011) showed, by two-dimensional RB simulations, that a different flow organization can lead to significant differences in the heat transport.

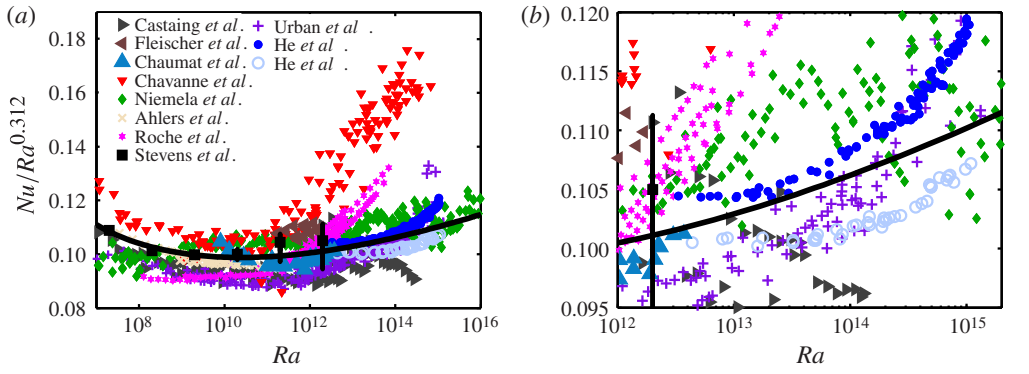

FIGURE 1. (Colour online) (*a*) *Nu* versus *Ra*. Unless stated otherwise the data are for $\Gamma = 1/2$. The experimental data from Castaing *et al.* (1989) are with wall corrections. The other experimental data are from Roche *et al.* (2010), Fleischer & Goldstein (2002), Chaumat, Castaing & Chilla (2002), Chavanne *et al.* (2001), Niemela *et al.* (2000), Ahlers *et al.* (2009*a*), Roche *et al.* (2010), Urban *et al.* (2011, 2012), the latter for $\Gamma = 1$; the two sets of experimental results of He *et al.* (2012) are for $T_U - T_m \lesssim -3K$ (filled circles) and $T_U - T_m \gtrsim +2K$ (open circles). DNS results from Stevens, Verzicco & Lohse (2010), Stevens, Lohse & Verzicco (2011) (squares) are also shown. (*b*) Zoom of the high-*Ra* regime.

Owing to technical difficulties, the physical properties and boundary conditions of the sidewall can only be controlled up to a certain degree in experiments. In addition, testing different sidewall configurations is a very time-consuming task as the entire sample has to be disassembled to replace the sidewall. On the other hand, direct numerical simulations (DNS), even though they cannot reach as high *Ra* as obtained in some experiments, offer a good possibility to study the influence of the physical properties and the boundary conditions at the sidewall as they can be exactly controlled. By comparing the differences between simulation of an RB sample with an adiabatic sidewall and of RB samples with several other sidewall configurations we aim to better understand the importance of sidewall effects.

The influence of the sidewall on the heat transport has been investigated before by Ahlers (2000), Roche *et al.* (2001*b*), Verzicco (2002) and Niemela & Sreenivasan (2003). The main conclusions are summarized in the review by Ahlers *et al.* (2009*c*). In short, the phenomenological models of Ahlers (2000) and Roche *et al.* (2001*b*) showed that one cannot fully account for the effect of the sidewall by simply subtracting the corresponding heat transferred to an empty cell. This was confirmed by Niemela & Sreenivasan (2003) who simulated an idealized two-dimensional convection problem with a conducting side surface and a fly-wheel-like structure in the bulk in order to mimic the mean flow sweeping the walls. Verzicco (2002) modelled the physical properties of the sidewall in three-dimensional DNS and found that, for usual sidewall thicknesses, the heat travelling from the hot to the cold plates directly through the sidewall is negligible due to the heat exchanged at the fluid/wall interface. In contrast, the modified temperature boundary conditions alter the mean flow, yielding significant *Nu* corrections in the low-*Ra* range. All these works suggested that the sidewall effects vanished for increasing *Ra*. However, recent experiments of Roche *et al.* (2010) and He *et al.* (2012) indicate that the properties and temperature boundary conditions of the sidewall are also important at higher *Ra*.

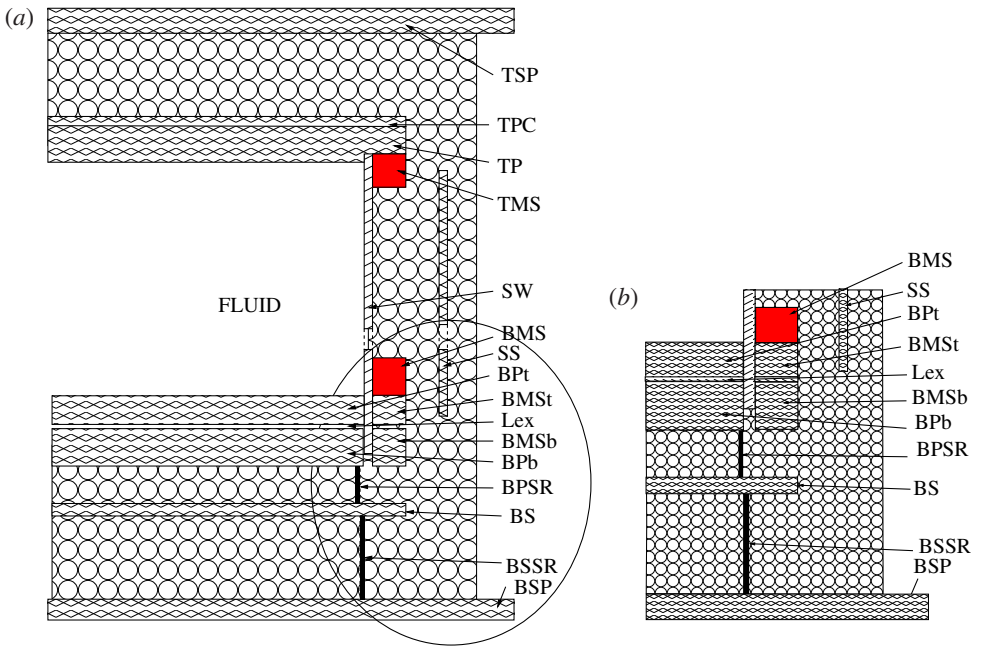

FIGURE 2. (Colour online) (*a*) Schematic diagram of the Göttingen RB setup (adapted from Ahlers *et al.* 2009*b*). From bottom to top, we show the bottom support plate (BSP), the bottom-shield support ring (BSSR), the bottom shield (BS), the bottom-plate support ring (BPSR), the bottom-plate bottom (BPb), the bottom-micro-shield bottom (BMSb), the Lexan plate (Lex), the bottom-micro-shield top (BMSt), the bottom-plate top (BPt), the bottom micro-shield (BMS indicated as a solid square), the side shield (SS) with its water cooling coil (WCC), the Plexiglas sidewall (SW), the top micro-shield (TMS, indicated as a solid square), the top plate (TP), the top-plate cover (TPC) and the top support plate (TSP). (*b*) Enlargement of the bottom-plate/sidewall assembly.

In this paper we will use DNS to study the influence of the physical properties of the sidewall and the temperature boundary conditions at the sidewall on the heat transport and the flow dynamics in RB convection.

First, we will discuss the numerical procedure employed in §2. In §3 we will show the difference between simulations with an adiabatic and an isothermal sidewall. This is an interesting comparison because in most experiments (Brown *et al.* 2005; Sun *et al.* 2005*a*; Ahlers *et al.* 2009*b*; Kunnen *et al.* 2011) the adiabatic temperature boundary condition is obtained by placing a temperature shield around the sidewall that is covered by a layer of insulation, see for example the sketch in figure 2(*a*) of the RB sample used in the Göttingen experiments. The temperature of the side shield is maintained at $T_M = T_c + \Delta/2$, where T_c is the temperature of the top plate, since this coincides with the mean temperature of the fluid in the bulk T_m (when the Oberbeck–Boussinesq approximation is fully valid). In figure 1(*b*) it is shown that the heat transport that is measured in the Göttingen experiments depends on $T_U - T_m$, where T_U is the temperature outside the RB sample. In order to investigate the possible influence of the temperature outside the cell we will consider different sidewall temperatures in §3. As a completely isothermal sidewall is an oversimplification of the experimental case, in §4 we will consider the case in which

only the bottom and top 1.5 % of the sidewall is kept at T_M and the rest of the sidewall is adiabatic. This case is based on the design of the Göttingen RB setup in which micro-shields with a temperature T_M are placed just above (below) the lower (upper) plate in order to prevent the insulated region between the sidewall and the side shield being influenced by the temperature of the horizontal plates (see figure 2). In order to be closer to the experimental situation we simulate the effect of the physical properties of the sidewall in §5 for some particular setups. In §6 we will also consider the effect of thermal shields at a fixed temperature and an external layer of insulating foam where porous convection occurs. Finally, in §7 a brief account of the changes induced in the flow dynamics by the presence of a non-ideal sidewall is given. We will conclude the paper with a short summary and some closing remarks. An Appendix has been added at the end of the paper with two tables containing the most relevant results of all the numerical simulations presented and discussed in this study.

2. Numerical procedure

In order to simulate the physical properties of the sidewall we solve the non-dimensional Navier–Stokes equations within the Boussinesq approximation

$$\frac{\mathrm{D}\boldsymbol{u}}{\mathrm{D}t} = -\boldsymbol{\nabla} P + \left(\frac{Pr}{Ra}\right)^{1/2} \nabla^2 \boldsymbol{u} + \theta \widehat{\boldsymbol{z}}, \quad \boldsymbol{\nabla}\cdot\boldsymbol{u} = 0 \qquad \text{on } V_f, \tag{2.1}$$

$$\frac{\mathrm{D}\theta}{\mathrm{D}t} = \frac{1}{(PrRa)^{1/2}} \frac{\rho_f C_{pf}}{\rho C} \boldsymbol{\nabla}\cdot\left(\frac{\lambda}{\lambda_f}\boldsymbol{\nabla}\theta\right) \qquad \text{on } V, \tag{2.2}$$

where V_f is the fluid domain $0 \leqslant z \leqslant L$, $0 \leqslant r \leqslant R_f$, and $0 \leqslant \phi \leqslant 2\pi$ with ϕ the azimuthal coordinate, and V ($0 \leqslant z \leqslant L$, $0 \leqslant r \leqslant R_w$, and $0 \leqslant \phi \leqslant 2\pi$) the total domain (see figure 3). Also, ρ, C and λ are, respectively, density, specific heat and thermal conductivity and they assume the values of the fluid (ρ_f, C_{pf} and λ_f with $k_f = \lambda_f/(\rho_f C_{pf})$) or of the sidewall ($\rho_w$, C_w and λ_w) depending on the specific point in the domain. Note that the physical properties of the sidewall are only incorporated in the simulations presented in §§5–7. In the simulations presented in §§3 and 4 the physical properties of the sidewall are not taken into account by setting $R_f = R_w$, which sets the sidewall thickness to zero. It is worth mentioning that as the temperature field is solved on the whole domain V no temperature boundary condition is required at the solid/fluid interface $r = R_f$. Instead the isothermal or adiabatic temperature boundary condition is imposed at the 'dry' sidewall surface $r = R_w$. A third possibility is to have a 'mixed temperature boundary condition' at the sidewall, i.e. isothermal for $0 \leqslant z \leqslant \Lambda$ and $L - \Lambda \leqslant z \leqslant L$ and adiabatic in between. This configuration mimics one particular feature of the apparatus of Ahlers *et al.* (2009*c*) as will be discussed later.

As indicated in figure 3, at the lower and upper plates, respectively, the temperatures T_h and T_c are prescribed so that they are modelled as isothermal surfaces. This implies that in our simulations the temperature difference Δ is imposed and the heat flux entering the fluid Q_f is measured by the non-dimensional Nusselt number $Nu = Q_f L/(\lambda_f \Delta)$; in the present paper the heat flux Q_f in the Nusselt number definition has been computed from the temperature gradient at the lower (hot) and upper (cold) plates of surface S, $Q_f = \int_0^{2\pi}\int_0^{R_f} \lambda_f \boldsymbol{\nabla}\theta\cdot\boldsymbol{n}\,\mathrm{d}S$. This situation is similar to some of the high-Ra experiments in which the temperature of the plates is kept constant (e.g. Ahlers *et al.* 2009*a*,*b*; Funfschilling *et al.* 2009), while other high-Ra experiments (Niemela *et al.* 2000, 2001; Niemela & Sreenivasan 2006) use an imposed heat flux at the lower plate and measure the temperature difference Δ; also in this case the

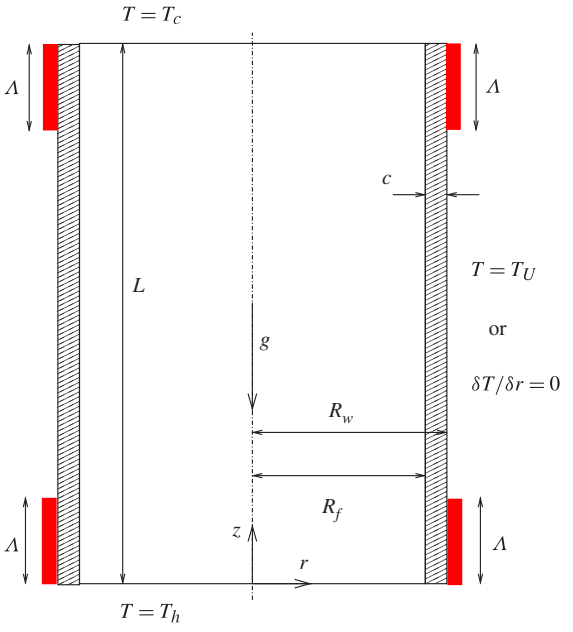

FIGURE 3. (Colour online) Sketch of the numerical setup of the problem: the upper and lower boundaries are isothermal and no-slip. The sidewall has a thickness $c = R_w - R_f$ and its 'dry' side at $r = R_w$ can be either adiabatic $\partial T/\partial r = 0$ or isothermal at a temperature $T = T_U$; there is also the possibility of having an isothermal boundary condition for the portions of the sidewall closest to the plates ($0 \leqslant z \leqslant \Lambda$ and $L - \Lambda \leqslant z \leqslant L$) while the rest of the sidewall is adiabatic. This will be referred to as a 'mixed boundary condition'. The 'wet side' of the sidewall ($r = R_f$) is no-slip while its temperature is not a boundary condition but part of the solution of (2.2) (conjugate heat transfer problem). When $c \neq 0$ the sidewall has thermal properties (density, specific heat and thermal conductivity) different from the fluid while for $c = 0$ the sidewall is a simple boundary condition for velocity and temperature. Note that the hot and cold isothermal surfaces of the plates also extend below and above the sidewall when its thickness is not zero.

results are normalized through the Nusselt number. Although we note that Johnston & Doering (2009) and Stevens *et al.* (2010) have shown that, regardless of the imposition of Δ or Q_f, the same Nu and the same Nu versus Ra relation is obtained (for high enough Rayleigh numbers) Nu and Q_f are not exactly the same quantity and changes in one do not necessarily imply changes in the other.

It is worth mentioning that for the simulations with finite-thickness sidewall the isothermal plates extend below and above the sidewall (see figure 3); therefore some heat is forced through the lateral wall even if only the flux entering and leaving the fluid layer is accounted for in the evaluation of the Nusselt number. This is trivial to achieve in numerical simulations by only considering the 'wet' surfaces in the computation of Nu. In contrast, in laboratory experiments the total heat entering the setup and the plates temperature difference are measured and disentangling the heat crossing only the fluid from the parasite currents is impossible. An initial naive approach consisted of subtracting the heat current measured in an empty cell from that actually crossing the setup with the fluid; this correction, however proved to be insufficient since it disregarded the conjugate heat transfer between the fluid and the lateral wall (Ahlers 2000; Roche *et al.* 2001*b*). Indeed, numerical simulations by

Verzicco (2002) showed that some heat was dynamically exchanged between fluid and sidewall when the latter had its own thermal properties and thickness and *ad hoc* corrections were derived to properly account for this effect (Ahlers 2000; Roche *et al.* 2001*b*; Verzicco 2002; Niemela & Sreenivasan 2003).

In this paper the discussion of the results will always use the Nusselt numbers computed only for the fluid, although some comments on the total heat entering the setup will be given in the Appendix.

In equations (2.1)–(2.2), $\widehat{\boldsymbol{z}}$ is the unit vector pointing in the opposite direction to gravity, $\mathrm{D}/\mathrm{D}t = \partial_t + \boldsymbol{u} \cdot \boldsymbol{\nabla}$ the material derivative, $\boldsymbol{u}$ the velocity vector with no-slip boundary conditions at all walls, and θ the non-dimensional temperature, $0 \leqslant \theta \leqslant 1$. The equations have been made non-dimensional by using the length L, the temperature difference Δ, and the free-fall velocity $U = \sqrt{\beta g \Delta L}$. These equations have been written in a cylindrical coordinate frame and discretized on a staggered mesh by central second-order-accurate finite-difference approximations. The numerical method is described in detail by Verzicco & Orlandi (1996), Verzicco & Camussi (1997) and Verzicco (2002). In this paper we present results for $2 \times 10^6 < Ra < 2 \times 10^{10}$ and $Pr = 0.7$ (i.e. gas) in an aspect ratio $\Gamma = 1/2$ sample.

In Stevens *et al.* (2010) we investigated the resolution criteria that should be satisfied in a fully resolved DNS and Shishkina *et al.* (2010) determined the minimal number of nodes that should be placed inside the boundary layers (BL). In Stevens *et al.* (2011) we showed that a $769 \times 193 \times 769$ grid is sufficient to properly resolve a simulation at $Ra = 2 \times 10^{10}$. Here we have used a resolution of $769 \times 257 \times 769$ for the simulations at $Ra = 2 \times 10^{10}$. The increased number of radial nodes was used to have a proper resolution in the thermal BL that is formed along an isothermal sidewall or a boundary with physical properties. A proportionally increased radial resolution was used at lower Ra where simulations could be run to test the effects of the resolution on the heat transfer. For $2 \times 10^7 \leqslant Ra \leqslant 2 \times 10^9$ the flow could be simulated with over-resolved meshes (up to 50 % in each direction). These resolution tests always gave Nu within a few percent of the values obtained with the reference resolution and the difference decreased for increasing Ra. This observation gives us confidence that the results are reliable and can be used for the flow analysis. Finally, we emphasize that for lower Ra (up to $Ra \approx 2 \times 10^8$) the results of our code agree well with completely independently written codes by Shishkina & Thess (2009), Hébert *et al.* (2010) and Scheel, Kim & White (2012), and also agree well with experimental results.

Before starting the discussion of the results we wish to point out that although from figure 1 it is evident that the largest differences among the experiments show for $Ra \geqslant 10^{11}$, running many simulations at these large Ra is not feasible due to limitations of the computational resources. As a compromise we have restricted our investigation to the range $2 \times 10^7 \leqslant Ra \leqslant 2 \times 10^{10}$ and whenever possible we have exaggerated the non-standard features (temperature boundary conditions, wall thicknesses, etc.) in order to make their effects on the flow already visible at lower Ra.

3. Isothermal sidewall

Figure 4 shows a visualization of the instantaneous temperature field at $Ra = 2 \times 10^8$ in a $\Gamma = 1/2$ sample when the sidewall is adiabatic and when it is kept at the constant temperature T_M. The figure shows that the difference between the two cases is the formation of a thermal BL along the sidewall when it is isothermal and this is most pronounced close to the horizontal plates. Figures 5(*a*) and 6 show that at relatively

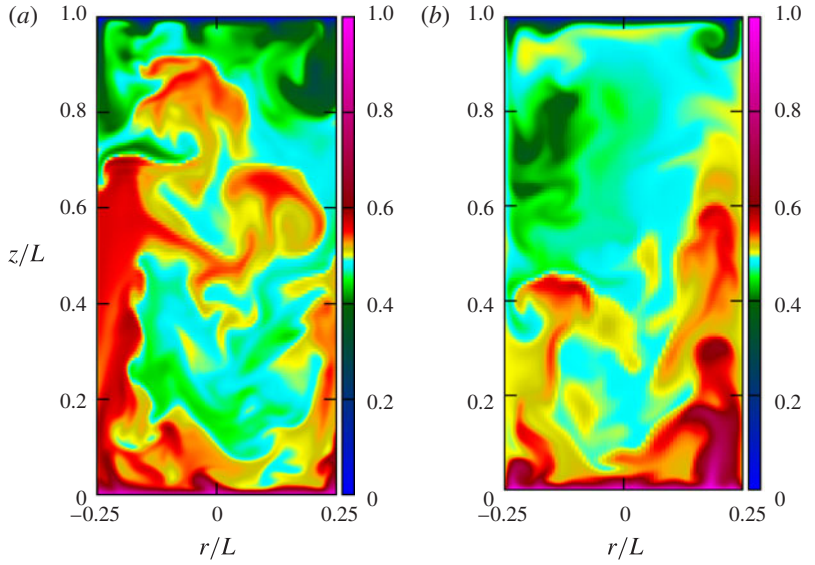

FIGURE 4. Visualization of instantaneous temperature field at $Ra = 2 \times 10^8$ and $Pr = 0.7$ in a $\Gamma = 1/2$ sample with an (a) adiabatic and (b) isothermal sidewall at T_M. Note the formation of the thermal BLs along the sidewall when the sidewall is isothermal.

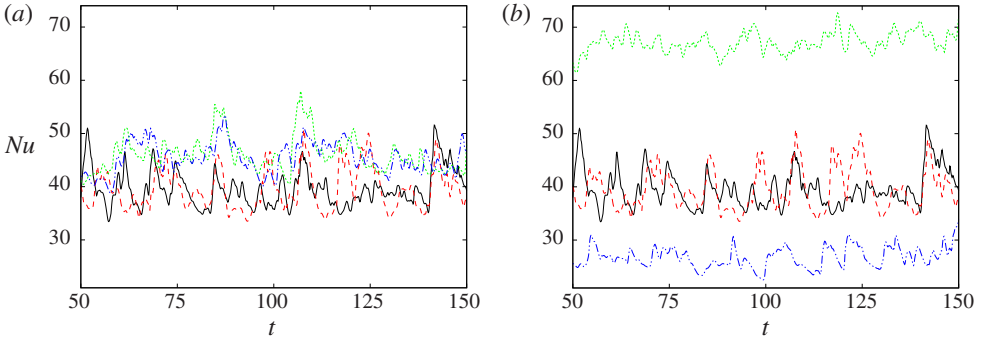

FIGURE 5. (Colour online) Nu at the bottom (–·–· and blue) and top plate (· · · · · · and green) as function of time for $Ra = 2 \times 10^8$ and $Pr = 0.7$ in a $\Gamma = 1/2$ sample when the temperature of the sidewall is kept at (a) $T_U = T_c + \Delta/2 = T_M$ and (b) $T_U = T_c + 0.75\Delta$ ($T_U - T_m = 0.071\Delta$). The heat transfer at the bottom (—— and black) and top (- - - - and red) plates for a reference simulation with adiabatic sidewall is given in both figures. The time t is in non-dimensional units L/U.

low Ra the heat flux is larger when the sidewall is isothermal than when the sidewall is adiabatic, even though the time-averaged heat flux through the entire sidewall is zero. However, locally there is a heat flux from the fluid to the sidewall in the lower half of the sample and vice versa in the top half. Because part of the heat current avoids the thermal resistance of the fluid in this way the heat transport measured at the horizontal plates is higher in the case of isothermal sidewalls. Figure 6 shows that the difference between the heat transport measured with an adiabatic sidewall and with

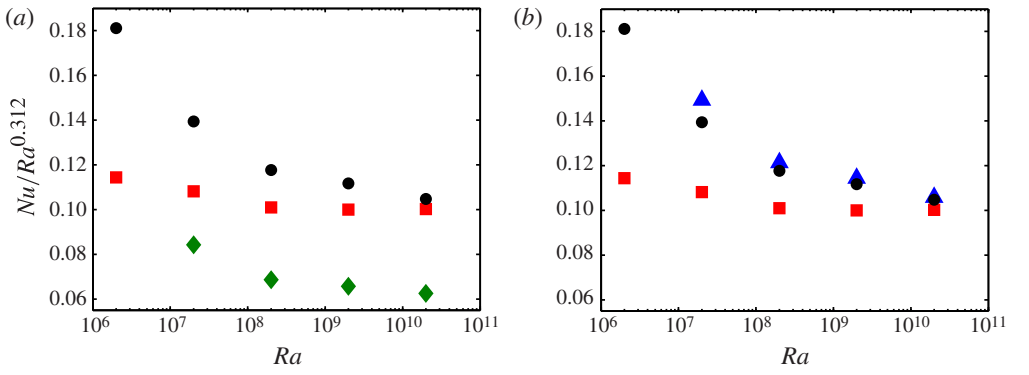

FIGURE 6. (Colour online) The heat transport in an RB sample with an adiabatic sidewall (squares) and a sidewall kept at $T_U = T_M$ (circles). In (*a*) these results are compared with simulations in which the sidewall temperature is $T_U = T_c + 0.75\Delta$ ($T_U - T_m = 0.071\Delta$), indicated by diamonds, and (*b*) shows the results for the simulations in which the lower and upper 1.5 % of the sidewall are kept at $T_U = T_M$ and the rest of the sidewall is adiabatic, indicated by triangles. Note that up to $Ra = 2 \times 10^{10}$ the error bar of Nu is smaller than the symbol size.

a sidewall kept at T_M decreases with increasing Ra. The reason is that with increasing Ra the temperature becomes more isothermal in the bulk. Figure 7 confirms that the azimuthally and time-averaged temperature close to the sidewall, more precisely at $r = R - \delta_\theta$, where $\delta_\theta = L/(2Nu)$ is the thermal BL thickness measured at the horizontal plates, becomes close to T_M just outside the thermal BLs and this effect is more pronounced at higher Ra. In addition, the BL thickness decreases with increasing Ra and therefore the fraction of the heat current that can avoid the thermal resistance of the fluid by going through the sidewall decreases with increasing Ra. This statement can be made more quantitative by observing the temperature profiles of figure 7(*c*,*d*) (isothermal sidewall) and computing the 'temperature defect' as $D = (1/L)\int_0^L |T(z) - T_m| \mathrm{d}z$, which is a measure of how much the fluid layer next to the sidewall deviates from the isothermal condition $T(z) = T_m$. We have obtained the values $D = 5.0 \times 10^{-2}$, 3.4×10^{-2}, 2.3×10^{-2} and 1.5×10^{-2}, respectively, for $Ra = 2 \times 10^7$, 2×10^8, 2×10^9 and 2×10^{10}. The same quantity computed for the profiles of figure 7(*a*,*b*) (adiabatic sidewall) yields $D = 8.0 \times 10^{-2}$, 5.2×10^{-2}, 3.8×10^{-2} and 2.6×10^{-2} (again for $Ra = 2 \times 10^7$, 2×10^8, 2×10^9 and 2×10^{10}) confirming that, in this second case, the flow is less isothermal. Nevertheless, the sidewall being perfectly adiabatic, no parasite heat currents can be produced through the sidewall.

On account of the above scenario nearly the same heat transport is already measured in an RB sample with an adiabatic sidewall and an isothermal surface at T_M when $Ra = 2 \times 10^{10}$.

In the Göttingen experiments (Ahlers *et al.* 2009*c*) the heat transport measurements have shown a relevant dependence on $T_U - T_m$, where T_U indicates the temperature outside the RB sample and T_m the average fluid temperature in the sample. As an aside we note that in a laboratory experiment T_m is not determined as a volume average of the temperature field but rather as a time average of a pointwise temperature measurement, or a series of measurements, at a vertical position halfway between the plates. It is worth mentioning that it is not at all trivial to decide how an external temperature T_U is 'felt' by the 'dry' surface of the sidewall because of

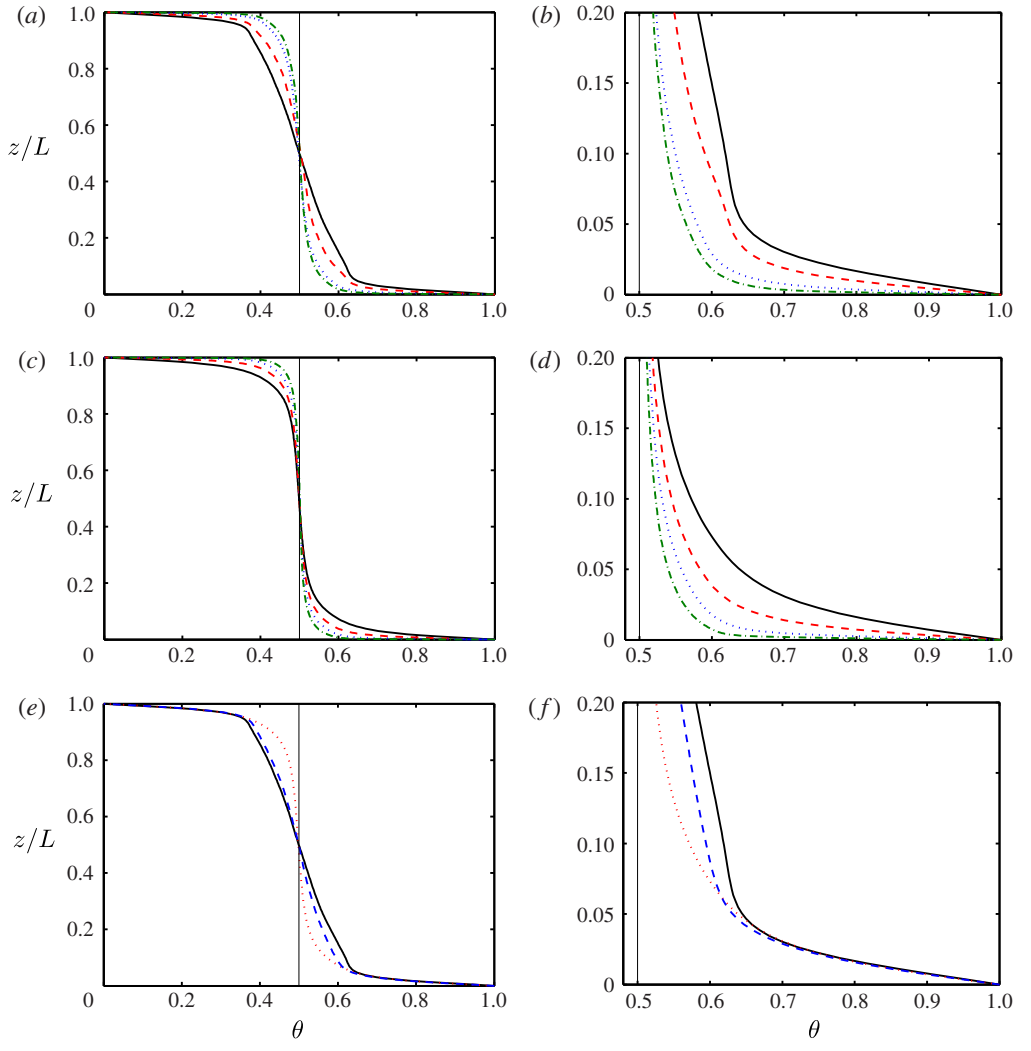

FIGURE 7. (Colour online) The temperature profiles at $r = R - \delta_\theta$ as a function of the height when the sidewall is adiabatic (*a,b*) and isothermal at T_M (*c,d*), for different Ra: —— , $Ra = 2 \times 10^7$; - - - - , $Ra = 2 \times 10^8$; · · · · · · , $Ra = 2 \times 10^9$; –·– , $Ra = 2 \times 10^{10}$. In (*e,f*) temperature profiles are compared for an adiabatic sidewall (——), a sidewall at T_M (· · · · · ·), and the model sidewall (T_M for $0 \leqslant z/L \leqslant 0.015$ and $0.985 \leqslant z/L \leqslant 1$ and adiabatic for $0.015 < z/L < 0.985$) (- - - -) at $Ra = 2 \times 10^7$. The plots on the left (*a–c*) show the profiles over the entire domain while the plots on the right (*d–f*) are for the region close to the bottom plate.

the complex interaction between the porous convection in the insulating foam and the isothermal surfaces of the various shields (see figure 2). Nevertheless, in a first attempt to model this effect we have changed the temperature of the sidewall to a value different from T_M. Figure 5(*b*) shows that the heat transport at the bottom and top plate is different when the temperature of the sidewall is different from T_M, because then a net heat flux is generated through the sidewall. Using geometrical arguments one can show that the relation between the heat flux at the bottom Nu_h

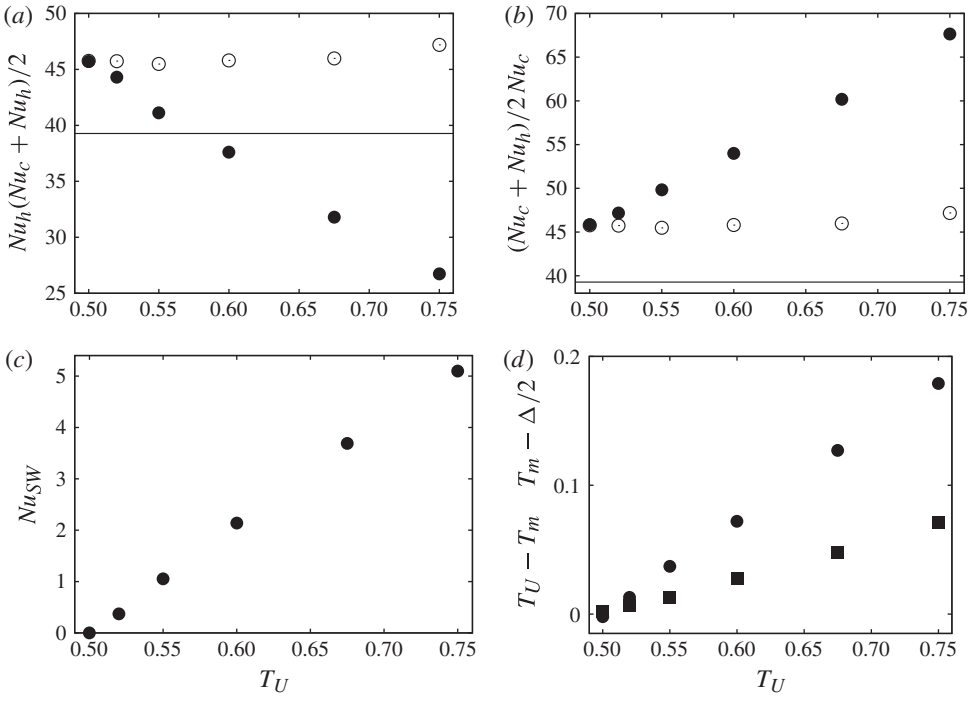

FIGURE 8. *Nu* versus T_U at $Ra = 2 \times 10^8$: (*a*) at the bottom plate and (*b*) at the top plate (solid circles); open circles in (*a,b*) show the average of the top and bottom values. (*c*) *Nu* versus T_U through the sidewall. (*d*) The mean temperature $T_m - \Delta/2$ (circles) and $T_U - T_m$ (squares) as functions of T_U.

and top plate Nu_c is given by

$$Nu_h + \frac{4}{\Gamma} Nu_{sw} = Nu_c, \tag{3.1}$$

where Nu_{sw} is the heat flux through the sidewall.

Figure 8 shows the time-averaged heat flux at the bottom and top plates and through the sidewall as function of the sidewall temperature for $Ra = 2 \times 10^8$ and $Pr = 0.7$. The figure shows that increasing the sidewall temperature results in a decrease of the heat transport measured at the bottom plate, but in an increase of the heat flux through the sidewall and the top plate, as is predicted by the relation (3.1). However, we note that $(Nu_h + Nu_c)/2$ stays approximately constant with T_U. This happens because the warmer sidewall warms up the fluid in the lower part of the cell and thereby decreases the heat flux that has to be supplied by the bottom plate. In order to compare these results with the Göttingen experiments we need to know $T_U - T_m$ for the different cases. In a first rough attempt to compare the simulations with the experiments we take for the temperature outside the cell T_U the temperature of the sidewall. Figure 8(*d*) shows that $T_U - T_m$ increases when the sidewall temperature is increased. It is worth mentioning that as $Nu_h \neq Nu_c$ it must be decided whether the heat transfer measured at the bottom or at the top plate should be taken for the comparison. Because in the Göttingen experiments He *et al.* (2012) only measured the heat transfer at the bottom plate (via the supplied electrical power)

we decided to compare the Nu measurements with the heat transport at the bottom plate. In agreement with the experiments of He *et al.* (2012) figure 6(*b*) shows that a positive $T_U - T_m$ results in a lower heat transport over a wide Ra range. In this case the heat transport does not converge to the value measured in a cell with an adiabatic sidewall for higher Ra, because now the warmer sidewall generates a heat flux through the sidewall, as shown in figure 8(*c*).

4. Mixed sidewall boundary conditions

As anticipated, a completely isothermal sidewall is too crude an oversimplification of the actual experimental configuration. When we examine the design of the Göttingen RB sample in figure 2(*a*) in more detail we find that there are micro-shields placed just above (below) the bottom (top) plate that are kept at a temperature of T_M in order to prevent the temperature of the plates influencing the isolated region between the sidewall and the side shield. With the aim of being closer to the experimental situation we consider the sidewall area adjacent to these micro-shields to have a constant temperature and the rest of the sidewall as adiabatic, since there is a thick insulation layer between the sidewall and the side shield. Schematically, this configuration is shown in figure 3. The isothermal regions close to the bottom and top plates are kept at a temperature of T_M and have a height of $\Lambda = 0.015L$, which is based on the design of the Göttingen RB setup (He *et al.* 2012).

Figure 6(*b*) shows that, remarkably, the results from this model are almost the same as for the case in which the entire sidewall temperature is kept at T_M. The reason is that the fluid temperature close to the sidewall only differs significantly from T_M inside the thermal BLs and most of the heat flux through the sidewall is found in these regions, see figure 7(*c,d*). In fact, when we compare the thickness of the thermal BL with the height of the isothermal region of the sidewall ($\Lambda = 0.015L$) used in the model, we find that already for relatively low Ra the small isothermal sidewall regions are larger than the thermal BL thickness $\lambda_\theta = L/(2Nu)$, which is $0.0188L$ at $Ra = 2 \times 10^7$, $0.0106L$ at $Ra = 2 \times 10^8$, $0.0054L$ at $Ra = 2 \times 10^9$, and $0.0029L$ at $Ra = 2 \times 10^{10}$. Thus in the model the sidewall is isothermal within the thermal BL regions. Therefore the model result is very close to that obtained with a completely isothermal sidewall. We note that in experiments this region of the sidewall that is close to the horizontal plates is particularly challenging to control. In fact, in this region the sidewall and the horizontal plates meet and therefore it is impossible to completely prevent all spurious heat currents and deviations from the intended ideal problem.

5. Sidewall with physical properties

In this section we investigate the influence of a sidewall with finite thickness and physical thermal properties on the measured heat transport. There are several different ways to join the sidewall with the hot and cold plates at the bottom ($z = 0$) and top ($z = L$) surfaces. Here, in order to simplify the computation and the imposition of the boundary conditions, we have chosen to 'extend' the plates below and above the sidewall (see the sketch of figure 3). In this case the sidewall and the bottom and top plate are in direct contact. It is worth mentioning that this is only one among several different possibilities for coupling the sidewall with the plates and, although it might resemble the arrangement of the Oregon/Trieste experiment (Niemela *et al.* 2000), it has been motivated mainly by its computational simplicity. Another possibility could be that the sidewall extends below (above) the hot (cold) plate and surrounds it, which is close to the Grenoble and Brno setups (Roche *et al.* 2001*b*; Urban *et al.* 2012).

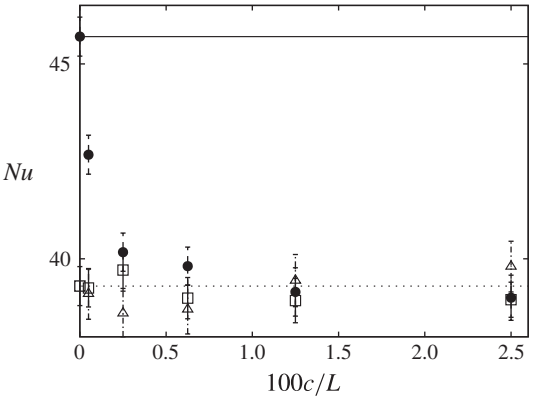

FIGURE 9. The heat transfer at $Ra = 2 \times 10^8$ as a function of sidewall thickness in a $\Gamma = 1/2$ sample with a stainless steel sidewall and filled with a gas at $Pr = 0.7$ (open triangles) for an adiabatic temperature boundary condition on the 'dry' side of the sidewall. The other symbols are the data for a Plexiglas sidewall and water as working fluid ($Pr = 7.0$): solid circles and open squares indicate, respectively, the results for an isothermal (T_M) and adiabatic temperature boundary condition on the 'dry' side of the sidewall. The dotted and solid lines indicate the adiabatic and isothermal (T_M) Nu for zero-thickness sidewalls, respectively.

The latter configuration has not been simulated in order to maintain the total amount of runs to a reasonable number. Other differences might come from flanges that are placed externally to the cell to join the sidewall with the plates or to connect different segments of the sidewall (Niemela *et al.* 2000); this would result in an effective wall thickness that is different from its nominal value.

We keep the fluid volume constant and vary the thickness of the sidewall by setting $R_w > R_f$, see figure 3. Differently from the results of the previous section, where only the Rayleigh and Prandtl numbers account for the thermal properties of the system, here we need also to specify the material properties of the sidewall in order to solve the conjugate heat transfer problem.

Initially, we consider a $\Gamma = 1/2$ sample with a stainless steel sidewall filled with gaseous helium ($Pr = 0.7$) at $T_M = 4.2$K. The corresponding material properties are $\rho_w/\rho_f = 485$, $C_w/C_{pf} = 0.00022$, and $\lambda_w/\lambda_f = 44.5$. In this case we compare with results from previous sections only for adiabatic temperature boundary conditions on the 'dry' side ($r = R_w$) of the stainless steel sidewall because in cryogenic helium experiments the convection cell is placed in a vacuum. Figure 9 shows that for the cryogenic helium/stainless steel combination the heat transport depends weakly on the sidewall thickness $c = R_w - R_f$, at least for $Ra = 2 \times 10^8$ and $Pr = 0.7$, which is in agreement with the results from Verzicco (2002) where this configuration has been analysed in detail. We consider further a $\Gamma = 1/2$ cell with a Plexiglas sidewall filled with water ($Pr = 7.0$), which has been adopted in several recent experiments (Xi & Xia (2008) with the material properties $\rho_w/\rho_f = 1.16$, $C_w/C_{pf} = 0.239$, and $\lambda_w/\lambda_f = 0.344$). For this configuration we use both adiabatic and constant-temperature boundary conditions on the 'dry' side ($r = R_w$) of the Plexiglas sidewall. Figure 9 shows that the heat transport as function of the sidewall thickness c depends on the temperature boundary condition on the 'dry' side of the sidewall. In particular, when the latter is isothermal, the heat transport decreases for increasing wall thickness; of

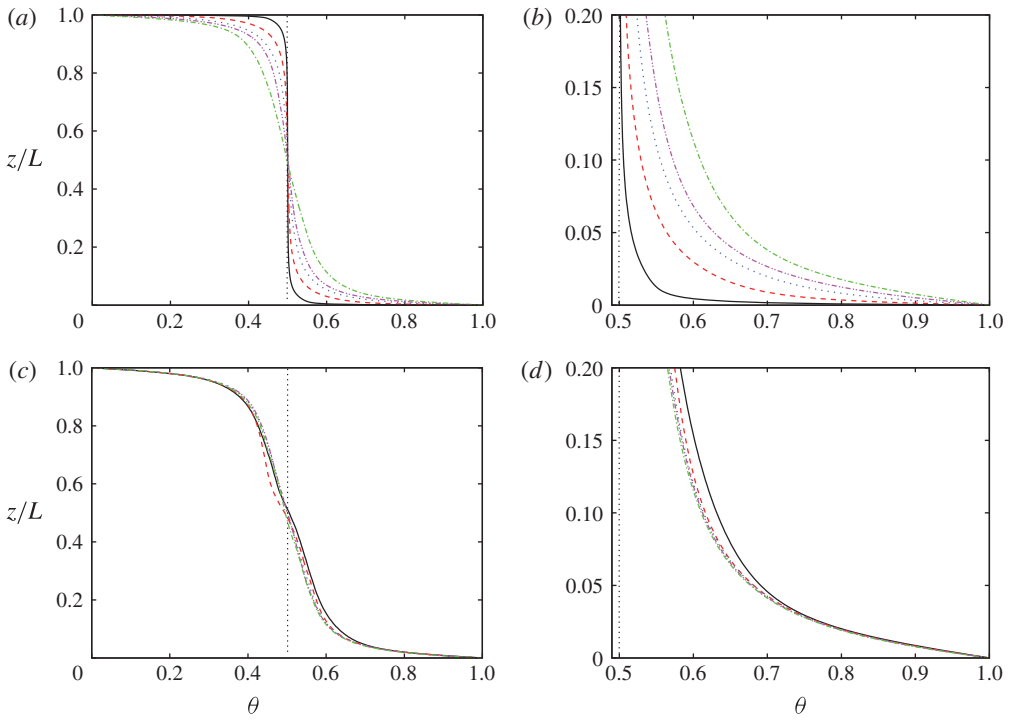

FIGURE 10. (*a,b*) The measured temperature profile at the sidewall/fluid interface as a function of the height when a container with a Plexiglas sidewall is filled with water ($Pr = 7.0$ and $Ra = 2 \times 10^8$) and the 'dry' surface of the sidewall is isothermal at temperature T_M. The colours indicate the different sidewall thicknesses: black $c = 0.005L$, red $c = 0.0025L$, blue $c = 0.0075L$, magenta $c = 0.0125L$ and green $c = 0.025L$. (*c,d*) The same as (*a,b*) but for an adiabatic 'dry' surface of the sidewall. The plots on the left-hand side (*a,c*) show the profiles over the entire domain and the plots on the right-hand side (*b,d*) show only the region close to the horizontal plate.

course as $c \to 0$, Nu recovers the value of figure 6 for an isothermal zero-thickness sidewall. For increasing c, owing to the isothermal boundary condition that moves further from the fluid/wall interface, Nu decreases and eventually drops slightly below the ideal (adiabatic zero-thickness sidewall) value since some of the heat escapes the fluid and flows through the sidewall. Figure 10 shows that this behaviour is related to the temperature of the sidewall at the fluid interface. The figure shows that when the sidewall is very thin and the 'dry' side of the sidewall is maintained at T_M the temperature at the fluid–wall interface is very close to T_M, except for a very small region close to the horizontal plates. This confirms that a very thin sidewall with these physical properties is indeed close to the case of a perfect isothermal sidewall. However, with increasing sidewall thickness the region in which the temperature of the sidewall at the fluid interface deviates from T_M increases significantly. This implies that for increasing c the radial heat flux through the sidewall is significantly lower than with a perfect isothermal surface and therefore it becomes closer to a sample with an adiabatic sidewall.

Also in this case it can be noted that when the 'dry' surface of the sidewall is adiabatic the effect of the sidewall thickness on the heat transfer is much less pronounced than with an isothermal boundary condition and it shows negligible

sensitivity to the sidewall thickness. The reason is that the temperature profiles at the fluid–wall interface and at $r = R_f - \delta_\theta$ are always close enough to prevent significant spurious heat fluxes and, owing to the reduced thermal conductivity of the wall, the temperature profiles do not change with c. Accordingly it is observed that the differences in Nu are of the order of 2–3 % and comparable to the actual precision of the heat transfer measurements ($\sim$2 %) of laboratory experiments. Nevertheless, as will be shown in § 7, relevant changes in the flow structure can be produced by changing the sidewall properties even when Nu is relatively unchanged.

We wish to point out that the results of figure 9 describe a general behaviour that holds regardless of the particular fluid/sidewall combinations even though the numbers presented here are specific for a cryogenic gaseous helium/stainless steel or ambient temperature Plexiglas/water setups. In fact, for the Göttingen experiments of He *et al.* (2012) with compressed SF_6 and a Plexiglas sidewall ($\rho_w/\rho_f = 11.705$, $C_w/C_{pf} = 2.004$, $\lambda_w/\lambda_f = 13.66$, and using $c/L = 0.0125$) at $Ra = 2 \times 10^8$ and $Pr = 0.7$ we find $Nu = 38.6$ using an isothermal boundary condition of T_M at the 'dry' side and using an adiabatic boundary condition at the 'dry' side. Note that this is below the value $Nu = 39.5$ computed for the ideal setup.

6. Isolation layer

All the results described above have been obtained assuming that the ambient temperature boundary conditions can be applied directly at the 'dry' side of the sidewall. Although this is already an improvement with respect to the direct imposition of the boundary condition at the fluid/wall interface, the real situation is far more complex because in between the sidewall and the ambient there are usually additional insulating layers and sometimes thermal shields (see figure 2). On the other hand we have already mentioned that the sidewall alone cannot prevent spurious radial heat fluxes from outside when the ambient temperature T_U is different from T_M and for this reason we have also simulated some cases in which the sidewall is covered by an insulating layer of foam and some thermal shields.

The simulated configuration is sketched in figure 11. The insulating foam (G. Ahlers, Personal Communication) has been assumed of open-cell type, to prevent its collapse when operating in pressurized environments as in the experiments of He *et al.* (2012), and therefore porous convection can occur. In order to model this phenomenon also we have resorted to an immersed boundary method (Fadlun *et al.* 2000) that modifies (2.1) to

$$\frac{\mathrm{D}\boldsymbol{u}}{\mathrm{D}t} = -\boldsymbol{\nabla} P + \left(\frac{Pr}{Ra}\right)^{1/2} \nabla^2 \boldsymbol{u} + \theta \widehat{\boldsymbol{z}} + \boldsymbol{f} \tag{6.1}$$

and allows fluid, solid and porous media to be handled with a single equation. In more detail, the forcing term $\boldsymbol{f}$ takes a different expression depending on the particular point in the domain:

(*a*) $\boldsymbol{f} = 0$ in the fluid so that (6.1) reduces to the Navier–Stokes equation;
(*b*) $\boldsymbol{f}$ has a value that ensures that $\boldsymbol{u} = 0$ within the solid parts (sidewall and thermal shields, see Fadlun *et al.* 2000 for more details);
(*c*) $\boldsymbol{f} = -\boldsymbol{u}/K$ in the insulating foam to allow for porous convection with pressure losses that depend on the porosity K (Navier–Stokes–Brinkman equation).

Note that (2.2) remains unmodified even if ρ, C and λ assume the value of the foam or the shields when the point is in those media.

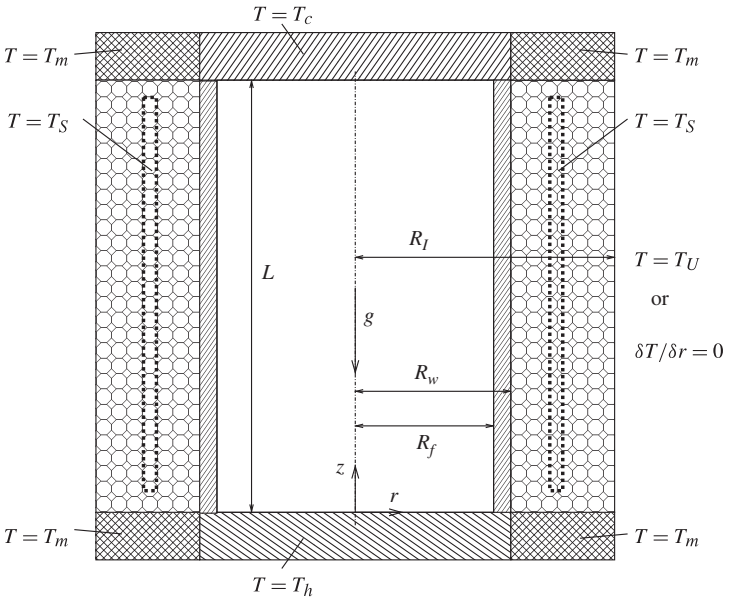

FIGURE 11. Sketch of the numerical setup for the cell with an external insulating layer and thermal shields; the upper and lower boundaries are isothermal. The sidewall has a thickness $c = R_w - R_f$ and the porous foam is $f = R_I - R_w$ thick; its 'external side' at $r = R_I$ can be either adiabatic $\partial T/\partial r = 0$ or isothermal at a temperature $T = T_U$. Within the foam volumes thermal shields with a prescribed temperature can be placed.

Looking at figure 11, and considering different combinations of materials, thicknesses of walls and layers, in addition to multiple shields at various positions, it is immediately clear that a complete parameter study is almost impossible owing to the enormous number of possible configurations. We have therefore considered only two cases, one with a layer of foam and without shields and another with three shields arranged as in He *et al.* (2012). For these simulations we have used the same resolutions as the previous cases at $Ra = 2 \times 10^8$ in the vertical and azimuthal direction. In contrast, the mesh in the radial direction had a larger number of radial nodes to simulate also the phenomena in the foam layer and in the thermal shields, and the computational points were non-uniformly distributed (by a third-order spline) to capture the boundary layers at the interfaces. Finally, the mesh had $193 \times 131 \times 257$ nodes in the azimuthal, radial and vertical directions (while the previous cases at $Ra = 2 \times 10^8$ were run on meshes of $193 \times 85 \times 257$ nodes).

For the first case we have assumed a foam layer of thickness $R_I - R_w = 0.1375L$ and with properties $\rho_I = 2\rho_f$, $C_I = C_{pf}$ and $\lambda_I = 5\lambda_f$ and a Plexiglas sidewall with thickness $c = 0.0125L$. For the non-dimensional porosity we have used the value $K = 10$ after having verified by preliminary simulations that the order of magnitude of the velocities within the foam was about fifty times smaller than that in the fluid. Figure 12(*a*) shows that the resulting Nu using an ambient temperature $T_U = T_M$ are consistent with the value of $Nu = 38.6$ found while modelling just the Plexiglas sidewall. Figure 12(*b*) shows that $T_U = T_c + 0.55\Delta$ gives $Nu_c = 40.1$ and $Nu_h = 37.1$ and both values are smaller than those of figure 8 for a similar T_U but without a sidewall with physical properties. Nevertheless the fact that $Nu_c > Nu_h$ suggests that, despite the layer of foam, some heat flux is entering the fluid through the sidewall

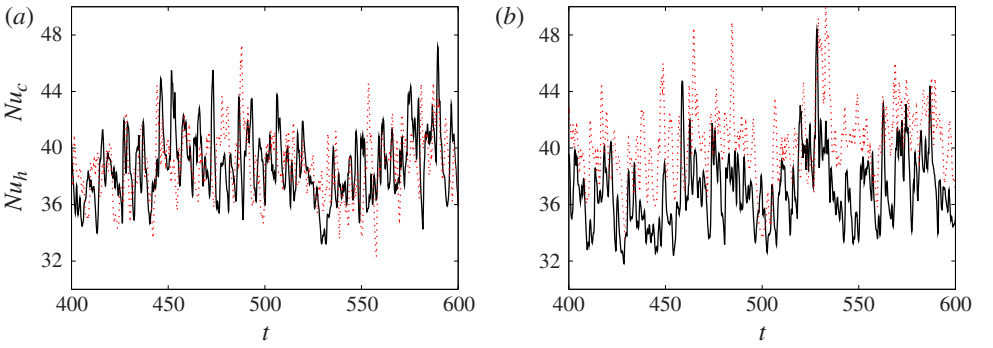

FIGURE 12. (Colour online) Time evolution of Nu at the hot (——) and cold (- - - -) plates for a flow at $Ra = 2 \times 10^8$ using compressed SF_6 ($Pr = 0.7$) with a Plexiglas sidewall of thickness $c = 0.0125L$ and a layer of insulating foam of thickness $R_I - R_w = 0.1375L$: (*a*) ambient temperature $T_U = T_M$, (*b*) ambient temperature $T_U = T_c + 0.55\Delta$.

and indeed it is confirmed by a direct computation. It is worth mentioning that this behaviour shows up only after a very long initial transient, of the order of $\sim 10^3$ time units at $Ra = 2 \times 10^8$, since it takes a long time before the system with a thick insulating foam layer reaches thermal equilibrium. Running similar cases at higher Ra is therefore unfeasible because the length of the initial transient will increase with increasing Ra, while the time step becomes smaller and the simulation cost per time step higher.

Figure 13 shows an instantaneous temperature snapshot for a flow at $Ra = 2 \times 10^8$ and $Pr = 0.7$ in a setup inspired by, but not identical to, the Göttingen experiment of He *et al.* (2012) with compressed SF_6 and a Plexiglas sidewall of thickness $c = 0.01L$. The ambient temperature is $T_U = T_c + 0.5\Delta = T_M$ and the setup includes also the top and bottom thermal micro-shields (BMS) and (TMS), tori of square cross-section $0.015L \times 0.015L$ at temperature T_M, and a side shield (SS) of thickness $0.01L$ at temperature T_M (see figure 2). For this configuration we have obtained a bulk temperature $T_m = 0.500$ that is indistinguishable from T_M and also the Nusselt numbers $Nu_c = 39.4$ and $Nu_h = 39.5$ agree with $Nu = 39.5$, which is measured in the 'ideal' RB cell with adiabatic sidewalls. It is interesting to note that nearly identical results for the Nusselt numbers and bulk temperature have been obtained in a setup as in figure 13 but with the surfaces at $z = 0$ and $z = L$ beyond the sidewall ($r > R_w$) at a constant temperature T_M.

The arrangement of thermal shields and isolation layers of figure 13 turned out to be very effective in preventing the effects of the external ambient temperature on the flow. In an additional simulation, in fact, the external temperature was set to $T_U = T_c + 0.675\Delta$ obtaining a bulk temperature $T_m = 0.499$ and the Nusselt numbers $Nu_c = 38.5$ and $Nu_h = 38.4$ that, though both smaller, agree within the statistical error ($\sim$3–4 %) with the reference value of $Nu = 39.5$.

It should be noted however that this result is extremely sensitive to the sealing between the cell and the thermal shields. In fact, in the setup of figure 13 the boundaries at $z = 0$ and $z = L$ are also no-slip beyond the sidewall ($r > R_w$) and the thermal shield SS extends vertically up to a distance of $0.015L$ from the horizontal plates. As a result the foam in the volume in between the sidewall and the thermal side shield is almost closed. Hence the velocities in the foam are more than hundred

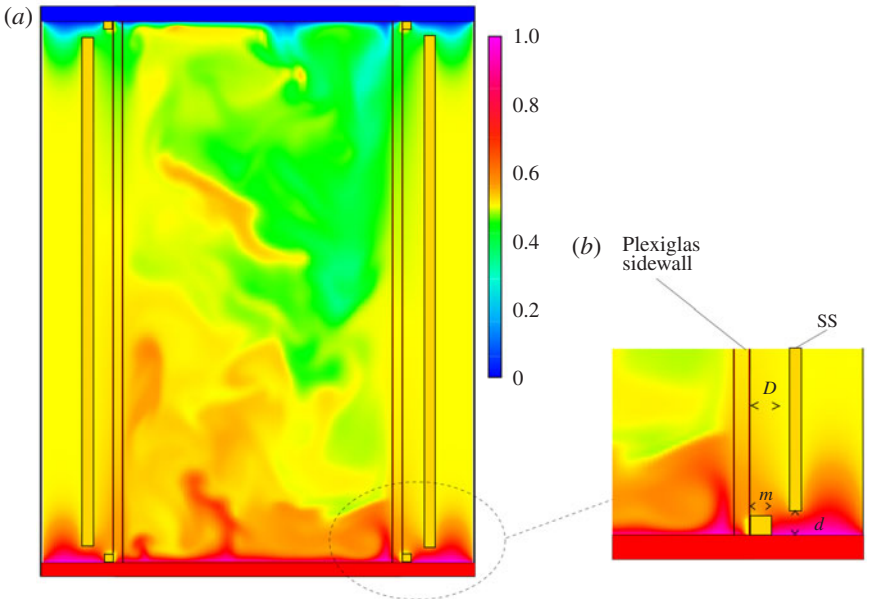

FIGURE 13. Instantaneous snapshot of the temperature field at $Ra = 2 \times 10^8$ and $Pr = 0.7$ for a setup with compressed SF_6 and a Plexiglas sidewall of thickness $c = 0.01L$. The ambient temperature is $T_U = T_c + 0.5\Delta$. This setup reproduces the micro-thermal shields BMS and TMS, toroidal rings of square cross-section $m \times m$ with $m = 0.015L$, at temperature T_M and the side shield SS, also at T_M. The side shield has a thickness of $0.01L$, a distance from the 'dry' side of the sidewall equal to $D = 0.03L$ and a distance from the bottom and top boundaries of $d = 0.015L$. This setup is inspired by the Göttingen experiment sketched in figure 2. Note that in this particular setup, the portion of the upper and lower surfaces ($z = 0$ and $z = L$) outside the sidewall ($r \geqslant R_w$) are set at the temperature T_M. On the right there is a detail of the sidewall, plate and shields junction. Note that the lower plate is conventionally coloured red while the fluid at the highest temperature $\theta = 1$ is indicated by magenta.

times smaller than in the fluid. In another simulation we have reduced the vertical length of the side shield so that it extended between $0.06L \leqslant z \leqslant 0.94L$ instead of the range $0.015L \leqslant z \leqslant 0.985L$ of the previous case. Owing to this small change in the shield extension the bulk temperature was slightly raised to $T_m = 0.507$, with an uncertainty below 1%, which is in the same direction as the results of figure 8(*d*). The Nusselt numbers, however, remained equal to the ideal *Nu* within the statistical uncertainty (∼3–4%) and further conclusions cannot be drawn.

Despite the effort in setting up a numerical simulation close to the Göttingen laboratory experiment of He *et al.* (2012) there are still details that make the two samples slightly different. In the latter case the volume between the sidewall and the shield SS is sealed by a film of lexan. In addition, direct contact between the top and bottom plates and the micro-shields (BMS, TMS) is prevented by another layer of lexan (G. Ahlers, Personal Communication). Both details have not been included in the numerical simulations.

Based on the above results it is clear that the flow can be influenced by the details of the experimental apparatus outside the fluid region. Since the number of possible

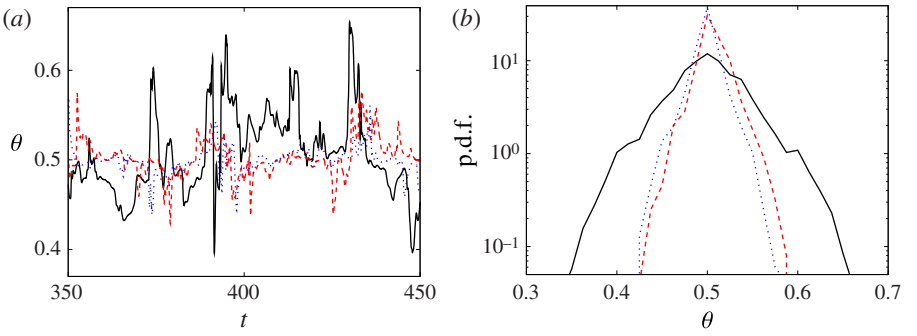

FIGURE 14. (Colour online) (*a*) Temperature time series sampled at $z = 0.5L$, $r = R_f - \delta_\theta$ (with $\delta_\theta = L/(2Nu)$), and $\phi = 0$ at $Ra = 2 \times 10^8$ and $Pr = 0.7$: —— , adiabatic sidewall; - - - - , isothermal sidewall; ····· , sidewall of finite thickness with isothermal 'dry' side ($c = 0.0125L$), Plexiglas/pressurized SF_6 combination). (*b*) Histograms of the time series of (*a*). In the adiabatic case the fluctuations are much larger.

combinations of shields, thicknesses, positions, materials and temperature boundary conditions is too large to be covered even by an *ad hoc* investigation, it would be advisable to run simulations of specific cases in order to test in advance a particular geometry. Nevertheless, as a general conclusion it can be said that the junction between the horizontal plates and the sidewall is particularly critical and also the use of thermal shields and their positioning, though generally beneficial, should be carefully considered.

7. Sidewall effects on the flow

In all the previous sections we focused on how the sidewall affects the heat transfer. In this section we show that the sidewall properties can also influence the flow structures and that this does not necessary have to be reflected in the Nusselt number.

From figure 10 it is already evident that a different sidewall temperature boundary condition can change the mean temperature profiles in the nearby flow region. However, these changes are only significant close to the horizontal plates where most of the (spurious) radial heat flux occurs. The situation is quite different for the temperature fluctuations since an adiabatic boundary allows for any fluctuation while an isothermal surface tends to anchor the fluid temperature to its own value. This behaviour is shown in figure 14 where temperature time series sampled by a probe at mid-height ($z = L/2$) and at the same radial distance from the boundary ($r = R_f - \delta_\theta$) are shown for an adiabatic, isothermal, and finite-thickness sidewall. The first evident difference for the first two cases is that, although both temperatures are fluctuating about the mean value T_M, the fluctuations are smaller for the constant-temperature sidewall, which is consistent with the above conjecture. The case with finite-thickness sidewall, with its own physical properties, shows fluctuations that are of the same order as those of the isothermal boundary even though the latter is not directly in contact with the fluid. In this case, however, the heat dynamics in the solid wall is coupled with that in the fluid and many different behaviours can be obtained by changing the solid and fluid properties.

We wish to stress, however, that this latter result depends on the temperature boundary condition on the 'dry' surface of the sidewall, on its thickness and on its

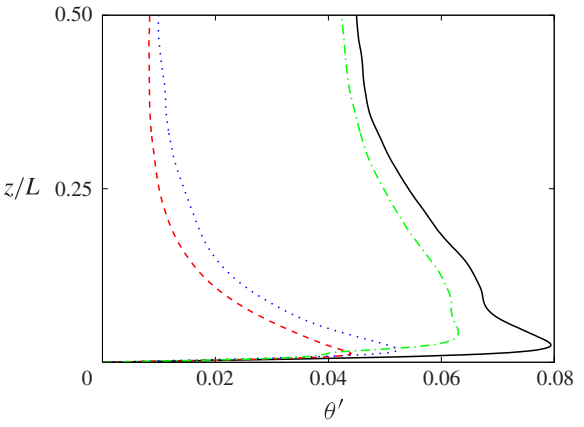

FIGURE 15. (Colour online) Time and azimuthally averaged vertical r.m.s. temperature profiles at a distance $\delta_\theta = L/(2Nu)$ from the 'wet' surface of the sidewall at $Ra = 2 \times 10^8$ and $Pr = 0.7$: —— , ideal adiabatic sidewall; - - - - , isothermal sidewall; –·– , mixed boundary conditions as in §4; · · · · · · , sidewall of finite thickness ($c = 0.0125L$, Plexiglas/pressurized SF_6 combination) with an isothermal temperature boundary condition on the 'dry' side.

physical properties through the ratios λ_w/λ_f, $\rho_w C_w/(\rho_f C_{pf})$ (see (2.2)). In fact, by varying the sidewall properties and its temperature boundary conditions it is possible to obtain, for the flow region next to the sidewall, any behaviour ranging from the absence of temperature fluctuations up to the maximum for the ideal adiabatic boundary with zero heat capacity.

The analysis in this section was motivated by the study of Ahlers *et al.* (2012) showing that the experimental measurements of wall-close vertical temperature profiles in the range $8 \times 10^{12} \leqslant Ra \leqslant 10^{15}$ behaved according to a logarithmic law even at the low end of *Ra*values where it was not expected since they did not belong to the ultimate regime predicted by Kraichnan (1962) and Grossmann & Lohse (2011). The data of the numerical simulations from Stevens *et al.* (2011) at $Ra = 2 \times 10^{12}$ not only confirmed the logarithmic temperature profiles but showed excellent agreement with the experimental fits (Ahlers *et al.* 2012). In contrast, the temperature fluctuation profiles in experiments and simulations, though both could be fitted by a logarithmic law, did not agree: in the numerical simulations the fluctuations were about five times larger than in the laboratory measurements. In a successive analysis part of the disagreement was found to be caused by the too large thermal inertia of the thermistors that acted as a low-pass filter on the temperature fluctuations (G. Ahlers, Personal Communication). Another part of the mismatch, however, should be ascribed to the different nature of the sidewall that, in the numerical simulation is ideal and adiabatic, therefore allowing for the maximal fluctuations, while in the experiment it is of finite thickness and made of Plexiglas. Figure 15 shows that indeed the sidewall has already altered the profiles of the temperature fluctuations at $Ra = 2 \times 10^8$ and that a wide range of possible behaviours can be obtained by changing the sidewall properties and the temperature boundary condition on the 'dry' side.

Before concluding this section we show that the sidewall can also play a key role in determining the mean flow structure. To this end have simulated an artificial example in which a gas is bounded on the side by a very conductive sidewall ($\rho_w C_w/(\rho_f C_{pf}) = 2925$, and $\lambda_w/\lambda_f = 1000$) of thickness $c = 0.0125L$. The thermal conductivity ratio is

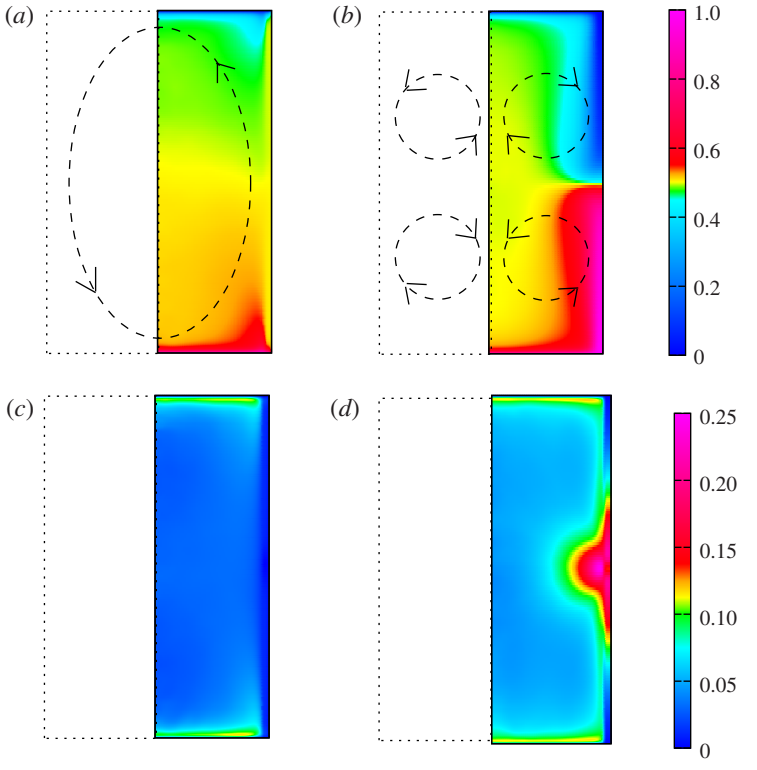

FIGURE 16. Time and azimuthally averaged temperature, (*a,b*), and r.m.s. temperature fluctuations, (*c,d*), for a flow at $Ra = 2 \times 10^8$ and $Pr = 0.7$ for a setup with finite-thickness sidewall ($c = 0.0125L$) with $\rho_w C_w/(\rho_f C_{pf}) = 2925$, and $\lambda_w/\lambda_f = 1000$: (*a,c*) an isothermal 'dry' surface of the sidewall; (*b,d*) an adiabatic temperature boundary condition. Note that the time- and azimuthal-average produces a single r–z meridional plane, the other half of the section is sketched by a dotted line for clarity. In (*a,b*) a drawing of the mean flow structure is also shown.

clearly exaggerated and this value is unlikely in a real experimental apparatus; here, however, we want to stress the effects on the mean flow structure of adiabatic and isothermal boundary conditions on the 'dry' surface of the sidewall and these are enhanced by a highly conductive material.

In figure 16 we show the mean and root-mean-square (r.m.s.) temperature maps at $Ra = 2 \times 10^8$ and $Pr = 0.7$ for two cases, with adiabatic and isothermal 'dry' sidewall. In the first case the mean flow consists of two vertically stacked counter-rotating toroidal vortices, while for the isothermal 'dry' boundary condition the large scale is the classical single-roll state. Figure 16(*c,d*) show that these flows produce completely different temperature fluctuations as argued at the beginning of this section.

Clearly, the reason for the generation of the two tori of figure 16(*b*) is the undesired temperature distribution along the sidewall that extends the plates along the vertical boundary, therefore also forcing the flow from the side. In contrast, when the 'dry' sidewall is forced to be isothermal at temperature T_M, the heat flowing from the horizontal plates to the sidewall can escape from the system directly through the isothermal surface without entering the fluid.

We wish to stress that the structures of figure 16(*a,b*) are not hysteretic configurations resulting from a particular initial condition but rather stable states to which the system relaxes. As a check, we have used the standard single-roll configuration of figure 16(*a*) as initial condition for the setup of figure 16(*b*) and we have verified that after a very long transient (of $\sim 800L/U$ time units) the flow undergoes a slow adjustment and eventually it recovers the two-tori configuration of figure 16(*b*). It is worth mentioning that despite the very different mean flow in both cases of figure 16 the bulk temperature was $T_m = T_M$ and the differences of Nu were well within those of isothermal and adiabatic sidewall temperature boundary conditions.

Finally, in this section, just as in other cases analysed in this paper, the thickness of the sidewall has been exaggerated in order to make its effect already evident at $Ra = 2 \times 10^8$ when the mean flow is intense and it dominates the flow dynamics. We find that, as Ra increases the large-scale circulation weakens and therefore it is likely that thinner sidewalls with reduced heat capacity would also be able to force a particular flow state.

8. Summary

We used direct numerical simulations (DNS) to investigate the influence of the physical properties and the temperature boundary conditions of the sidewall on the heat transport in Rayleigh–Bénard (RB) convection. The cases we considered are inspired by the experiments of Ahlers *et al.* (2009*b*), Xi & Xia (2008) and Niemela *et al.* (2000). He *et al.* (2012) found two different branches for the heat transport: a slightly higher heat transport is measured when $T_U - T_m$ is negative, where T_U is the temperature outside the cell and T_m is the average fluid temperature, and vice versa when $T_U - T_m$ is positive.

We show that keeping the temperature of the sidewall fixed at T_M leads to a higher heat transport at lower Ra, because part of the heat current circumvents the thermal resistance of the fluid by going through the sidewall. However, this effect disappears at higher Ra where the bulk becomes more isothermal and the heat flux through the sidewall decreases. In agreement with the experimental results we find that an increase of the sidewall temperature, with respect to the value T_M, leads to a lower heat transfer at the bottom plate. Just as in experiments this effect is visible over a large Ra regime; at least up to $Ra = 2 \times 10^{10}$, there are no indications that the effect decreases for increasing Ra. Subsequently, we argue that in the Göttingen RB setup the temperature boundary condition should be close to adiabatic in the centre region and close to a constant-temperature condition of T_M in the vicinity of the horizontal plates due to the use of the micro-shields. The heat transfer we measure at the bottom plate in this model is the same as the heat transfer that is obtained when the entire sidewall is kept at T_M. This shows that the sidewall region close to the horizontal plates is crucial, while this is particularly challenging region in experiments as the sidewall and the horizontal plates meet in this region and therefore it is impossible to completely prevent all heat currents in that region.

The flow dynamics is more complex when the sidewall is considered, with its thermal properties and thickness, because the heat dynamics in the fluid couples with that in the wall. For RB samples filled with water ($Pr = 7.0$) and with a Plexiglas lateral boundary, the Nusselt number shows little sensitivity to the sidewall thickness when its 'dry' surface is adiabatic. In contrast, when the 'dry' side of the sidewall is isothermal, the temperature at the fluid–wall interface becomes such that large heat

fluxes through the sidewall are generated. However these spurious fluxes decrease as the wall thickness increases and, for thick enough sidewalls ($c \geqslant 0.0075L$) the deviations of Nu are below 2–3 %.

As a proof-of-concept, resorting to the Navier–Stokes–Brinkman equations, we have simulated a case with an additional external insulation layer of foam, where porous convection can occur, and some others with the foam and several thermal shields. The former case showed that, apart from producing very long transients, the foam alone could not prevent the flow being affected by an ambient temperature T_U different from T_M. In contrast, the combined use of foam and thermal shields adequately prevented undesired effects. Nevertheless, it has also been shown that the shielding of the region next to the junction between plates and sidewall is really crucial and small changes in the shield position are already sensed by the flow at $Ra = 2 \times 10^8$.

We wish to point out that all the simulations with the foam and the shields were performed at $Ra = 2 \times 10^8$ owing to the augmented complexity of the problem that largely increased the computational time of the simulations. Although the results have given useful indications about some additional effects they have been obtained for a Rayleigh number that is few orders of magnitude below the range of the experiments ($Ra = 10^{11}$–10^{15}). The present results, therefore, should not be trivially applied to the experiments without further considerations on very high Rayleigh number flows.

Finally, it was shown that the sidewall not only affects the heat transfer but can also influence the temperature fluctuations and even the mean flow structure. Owing to the very large number of parameters that can influence the flow it is unfeasible to explore the complete phase space. By analysing some particular aspects, however, we hope to have shed some light on details that should be kept under control when designing a new setup or running an experiment.

Acknowledgements

We thank G. Ahlers for stimulating discussion and for providing data and details of his experiments. The presented simulations were performed on Huygens (DEISA (Distributed European Infrastructure for Supercomputing Applications) project), CASPUR (Inter-University Consortium for the Application of Super-Computing for Universities and Research), and HLRS (High Performance Computing Center Stuttgart). We gratefully acknowledge the support of Wim Rijks (SARA) and we thank the DEISA Consortium (www.deisa.eu), co-funded through the EU FP7 project RI-222919, for support within the DEISA Extreme Computing Initiative. R.J.A.M.S. was financially supported by the Foundation for Fundamental Research on Matter (FOM).

Appendix. Tables with the results of the simulations

In this Appendix we report the key data of the simulations performed in the paper; table 1 contains the data for the zero-thickness sidewall (see §§3 and 4). Table 2 summarizes the simulations with the finite-thickness sidewall with thermal properties of §5.

Following the papers by Ahlers (2000), Roche *et al.* (2001*b*), Verzicco (2002) and Niemela & Sreenivasan (2003) we can compute the total heat flowing through the hot plate as $Q_T = \int_0^{2\pi} \int_0^{R_w} \lambda \nabla\theta \cdot \boldsymbol{n}\, \mathrm{d}S$ and the heat going from the hot plate directly into the sidewall as $Q_w = \int_0^{2\pi} \int_{R_f}^{R_w} \lambda \nabla\theta \cdot \boldsymbol{n}\, \mathrm{d}S$, where λ is either the thermal conductivity of the fluid λ_f or of the sidewall λ_w depending on whether the point of the plate is in contact

Ra	SW (T_U)	T_m	Nu_h	Nu_c	Nu_{sw}
2×10^6	Adiab.	0.50	10.63	10.64	≈0
2×10^6	Isot. (0.5)	0.50	16.73	16.74	≈0
2×10^7	Adiab.	0.50	20.50	20.42	≈0
2×10^7	Isot. (0.5)	0.50	26.41	26.40	≈0
2×10^7	Isot. (0.75)	0.68	15.86	39.10	3.01
2×10^7	Mixed	0.50	28.03	28.00	≈0
2×10^8	Adiab.	0.50	39.50	39.60	≈0
2×10^8	Isot. (0.5)	0.50	45.70	45.83	≈0
2×10^8	Isot. (0.52)	0.51	44.31	47.13	0.37
2×10^8	Isot. (0.55)	0.54	41.12	49.83	1.02
2×10^8	Isot. (0.60)	0.57	37.60	54.00	2.14
2×10^8	Isot. (0.675)	0.63	31.80	60.17	3.69
2×10^8	Isot. (0.75)	0.68	26.73	67.65	5.04
2×10^8	Mixed	0.50	47.22	46.96	≈0
2×10^9	Adiab.	0.50	79.75	79.73	≈0
2×10^9	Isot. (0.5)	0.50	89.36	89.31	≈0
2×10^9	Isot. (0.75)	0.67	54.99	131.51	10.20
2×10^9	Mixed	0.50	90.56	91.21	≈0
2×10^{10}	Adiab.	0.50	173.10	173.48	≈0
2×10^{10}	Isot. (0.5)	0.50	171.58	171.16	≈0
2×10^{10}	Isot. (0.75)	0.68	102.28	277.51	22.41
2×10^{10}	Mixed	0.50	173.84	173.33	≈0

TABLE 1. Summary of the simulations performed for the configuration with 'zero-thickness' sidewall. The columns from left to right indicate the Rayleigh number (Ra); the sidewall temperature boundary condition, adiabatic (adiab.) or isothermal (isot.) and for the latter the imposed temperature (T_U); and the volume-averaged fluid temperature (T_m). Nu_h and Nu_c are, respectively, the Nusselt numbers computed as surface averages at the hot and cold plates. Nu_{sw} is the Nusselt number evaluated as surface average on the sidewall. All the simulations are performed at $Pr = 0.7$.

with the former or the latter. The heat entering the fluid layer is trivially $Q_f = Q_T - Q_w$ and it should be used to compute the Nusselt number. In laboratory experiments, only Q_T is available and, according to Ahlers (2000), the factors $f_w = Q_w/Q_T$ or $f_f = Q_f/Q_T$, if known from some model, could be used to correct the measured quantity Q_T to compute a corrected Nusselt number via $Nu_{corr} = f_f Q_T/S$.

In table 2 we report the factor f_f as obtained by the present numerical simulations in which Q_T and Q_f could be computed separately. We note that the case of cryogenic helium and $c/L = 0.0025$ agrees with the results of Verzicco (2002). The values obtained for the stainless steel/gaseous helium setup imply larger differences than those for the combination Plexiglas/water: this is not surprising on account of the bigger ratio of the thermal conductivities λ_w/λ_f of the former case. For the combination of Plexiglas and water the correction is bigger for isothermal boundary conditions on the 'dry' side of the sidewall than for the adiabatic case.

We also report the wall number $W = (4/\Gamma)(\lambda_w/\lambda_f)(c/L)$ and the correction factor $F = 1/[1 + f(W)]$ with $Nu_{corr} = FQ_T/S$, where $f(W) = [A^2/(\Gamma Nu)](\sqrt{1 + 2W\Gamma Nu/A^2} - 1)$ as defined by Roche *et al.* (2001*b*) with $A = 0.8$.

Pr	$(\rho C)_w/(\rho C_p)_f$	λ_w/λ_f	$100c/L$	SW (T_U)	T_m	Nu_h	Nu_c	f_f	W	F
0.7	0.107	44.5	0.05	Adiab.	0.50	39.04	39.22	0.964	0.178	0.926
0.7	0.107	44.5	0.25	Adiab.	0.50	38.70	38.51	0.877	0.89	0.827
0.7	0.107	44.5	0.625	Adiab.	0.50	38.82	38.51	0.784	2.225	0.743
0.7	0.107	44.5	1.25	Adiab.	0.50	39.56	39.32	0.594	4.450	0.665
0.7	0.107	44.5	2.5	Adiab.	0.50	39.68	39.95	0.210	8.900	0.580
7.0	0.277	0.344	0.05	Adiab.	0.50	39.37	39.24	0.999	0.0014	0.999
7.0	0.277	0.344	0.25	Adiab.	0.50	38.08	38.46	0.998	0.007	0.993
7.0	0.277	0.344	0.625	Adiab.	0.50	39.13	38.80	0.992	0.017	0.986
7.0	0.277	0.344	1.25	Adiab.	0.50	39.06	38.91	0.909	0.034	0.976
7.0	0.277	0.344	2.5	Adiab.	0.50	39.16	38.75	0.968	0.069	0.960
7.0	0.277	0.344	0.05	Isot. (0.5)	0.50	42.73	42.61	0.970	0.0014	0.999
7.0	0.277	0.344	0.25	Isot. (0.5)	0.50	40.25	40.12	0.938	0.007	0.997
7.0	0.277	0.344	0.625	Isot. (0.5)	0.50	39.73	39.89	0.919	0.017	0.986
7.0	0.277	0.344	1.25	Isot. (0.5)	0.50	39.26	39.08	0.927	0.034	0.976
7.0	0.277	0.344	2.5	Isot. (0.5)	0.50	38.86	39.15	0.891	0.069	0.960
0.7	23.45	13.66	1.25	Adiab.	0.50	38.71	38.55	0.899	1.366	0.790
0.7	23.45	13.66	1.25	Isot. (0.5)	0.50	38.54	38.67	0.213	1.366	0.790

TABLE 2. Summary of the simulations performed for the configuration with 'finite-thickness' sidewall with thermal properties. The columns from left to right indicate the Prandtl number (Pr); the ratio of the specific heat capacities (ρC) of wall and fluid; the ratio of their thermal conductivities (λ); the sidewall thickness (c); the 'dry surface' sidewall temperature boundary condition, adiabatic (adiab.) or isothermal (isot.) and for the latter the imposed temperature (T_U); and the volume-averaged fluid temperature (T_m). Nu_h and Nu_c are, respectively, the Nusselt numbers computed as surface averages at the hot and cold plates; f_f is the ratio of the heat flowing through the sidewall (Q_w) and the total heat (Q_T) imposed on the system. $W = (4/\Gamma)(\lambda_w/\lambda_f)(c/L)$ is the wall number and $F = 1/[1 + f(W)]$ with $f(W) = [A^2/(\Gamma Nu)](\sqrt{1 + 2W\Gamma Nu/A^2} - 1)$ as defined by Roche *et al.* (2001*b*). All the simulations are performed at $Ra = 2 \times 10^8$.

Finally we emphasize that the Nusselt number even if computed by $Nu = Q_f/S$ deviates substantially from the value Nu_{ideal} as it comes from a simulation with a zero-thickness adiabatic sidewall in the case of the isothermal sidewall boundary condition. Therefore, even if f were given by some reliable model it would not return the ideal Nusselt number owing to the changes produced in the flow by the conjugate heat transfer between the lateral boundary and the fluid layer.

REFERENCES

AHLERS, G. 2000 Effect of sidewall conductance on heat-transport measurements for turbulent Rayleigh–Bénard convection. *Phys. Rev.* E **63**, 015303.

AHLERS, G., BODENSCHATZ, E., FUNFSCHILLING, D., GROSSMANN, S., HE, X., LOHSE, D., STEVENS, R. J. A. M. & VERZICCO, R. 2012 Logarithmic temperature profiles in turbulent Rayleigh–Bénard convection. *Phys. Rev. Lett.* **109**, 114501.

AHLERS, G., BODENSCHATZ, E., FUNFSCHILLING, D. & HOGG, J. 2009*a* Turbulent Rayleigh–Bénard convection for a Prandtl number of 0.67. *J. Fluid Mech.* **641**, 157–167.

AHLERS, G., FUNFSCHILLING, D. & BODENSCHATZ, E. 2009*b* Transitions in heat transport by turbulent convection at Rayleigh numbers up to 10^{15}. *New J. Phys.* **11**, 123001.

AHLERS, G., FUNFSCHILLING, D. & BODENSCHATZ, E. 2011 Addendum to transitions in heat transport by turbulent convection at Rayleigh numbers up to 10^{15}. *New J. Phys.* **13**, 049401.

AHLERS, G., GROSSMANN, S. & LOHSE, D. 2009*c* Heat transfer and large-scale dynamics in turbulent Rayleigh–Bénard convection. *Rev. Mod. Phys.* **81**, 503–537.

BROWN, E., FUNFSCHILLING, D., NIKOLAENKO, A. & AHLERS, G. 2005 Heat transport by turbulent Rayleigh–Bénard convection: Effect of finite top- and bottom conductivity. *Phys. Fluids* **17**, 075108.

CASTAING, B., GUNARATNE, G., HESLOT, F., KADANOFF, L., LIBCHABER, A., THOMAE, S., WU, X. Z., ZALESKI, S. & ZANETTI, G. 1989 Scaling of hard thermal turbulence in Rayleigh–Bénard convection. *J. Fluid Mech.* **204**, 1–30.

CHAUMAT, S., CASTAING, B. & CHILLA, F. 2002 Rayleigh–Bénard cells: influence of plate properties. In *Advances in Turbulence IX* (ed. I. P. Castro, P. E. Hancock & T. G. Thomas), Barcelona: International Center for Numerical Methods in Engineering, CIMNE.

CHAVANNE, X., CHILLA, F., CHABAUD, B., CASTAING, B. & HEBRAL, B. 2001 Turbulent Rayleigh–Bénard convection in gaseous and liquid he. *Phys. Fluids* **13**, 1300–1320.

CHILLÀ, F., RASTELLO, M., CHAUMAT, S. & CASTAING, B. 2004 Long relaxation times and tilt sensitivity in Rayleigh–Bénard turbulence. *Eur. Phys. J.* B **40**, 223–227.

FADLUN, E. A., VERZICCO, R., ORLANDI, P. & MOHD-YUSOF, J. 2000 Combined immersed-boundary finite-difference methods for three-dimensional complex flow simulations. *J. Comput. Phys.* **161**, 35–60.

FLEISCHER, A. S. & GOLDSTEIN, R. J. 2002 High-Rayleigh-number convection of pressurized gases in a horizontal enclosure. *J. Fluid Mech.* **469**, 1–12.

FUNFSCHILLING, D., BODENSCHATZ, E. & AHLERS, G. 2009 Search for the 'ultimate state' in turbulent Rayleigh–Bénard convection. *Phys. Rev. Lett.* **103**, 014503.

GROSSMANN, S. & LOHSE, D. 2000 Scaling in thermal convection: A unifying view. *J. Fluid Mech.* **407**, 27–56.

GROSSMANN, S. & LOHSE, D. 2001 Thermal convection for large Prandtl number. *Phys. Rev. Lett.* **86**, 3316–3319.

GROSSMANN, S. & LOHSE, D. 2002 Prandtl and Rayleigh number dependence of the Reynolds number in turbulent thermal convection. *Phys. Rev.* E **66**, 016305.

GROSSMANN, S. & LOHSE, D. 2004 Fluctuations in turbulent Rayleigh–Bénard convection: The role of plumes. *Phys. Fluids* **16**, 4462–4472.

GROSSMANN, S. & LOHSE, D. 2011 Multiple scaling in the ultimate regime of thermal convection. *Phys. Fluids* **23** (4), 045108.

HE, X., FUNFSCHILLING, D., NOBACH, H., BODENSCHATZ, E. & AHLERS, G. 2012 Transition to the ultimate state of turbulent Rayleigh–Bénard convection. *Phys. Rev. Lett.* **108**, 024502.

HÉBERT, F., HUFSCHMID, R., SCHEEL, J. & AHLERS, G. 2010 Onset of Rayleigh–Bénard convection in cylindrical containers. *Phys. Rev.* E **81**, 046318.

JOHNSTON, H. & DOERING, C. R. 2009 Comparison of turbulent thermal convection between conditions of constant temperature and constant flux. *Phys. Rev. Lett.* **102**, 064501.

KRAICHNAN, R. H. 1962 Turbulent thermal convection at arbritrary Prandtl number. *Phys. Fluids* **5**, 1374–1389.

KUNNEN, R. P. J., STEVENS, R. J. A. M., OVERKAMP, J., SUN, C., VAN HEIJST, G. J. F. & CLERCX, H. J. H. 2011 The role of Stewartson and Ekman layers in turbulent rotating Rayleigh–Bénard convection. *J. Fluid Mech.* **688**, 422–442.

NIEMELA, J., SKRBEK, L., SREENIVASAN, K. R. & DONNELLY, R. 2000 Turbulent convection at very high Rayleigh numbers. *Nature* **404**, 837–840.

NIEMELA, J., SKRBEK, L., SREENIVASAN, K. R. & DONNELLY, R. J. 2001 The wind in confined thermal turbulence. *J. Fluid Mech.* **449**, 169–178.

NIEMELA, J. & SREENIVASAN, K. R. 2003 Confined turbulent convection. *J. Fluid Mech.* **481**, 355–384.

NIEMELA, J. & SREENIVASAN, K. R. 2006 Turbulent convection at high Rayleigh numbers and aspect ratio 4. *J. Fluid Mech.* **557**, 411–422.

NIEMELA, J. J. & SREENIVASAN, K. R. 2010 Does confined turbulent convection ever attain the 'asymptotic scaling' with 1/2 power? *New J. Phys.* **12**, 115002.

VAN DER POEL, E. P., STEVENS, R. J. A. M. & LOHSE, D. 2011 Connecting flow structures and heat flux in turbulent Rayleigh–Bénard convection. *Phys. Rev.* E **84**, 045303(R).

ROCHE, P. E., CASTAING, B., CHABAUD, B. & HEBRAL, B. 2001*a* Observation of the 1/2 power law in Rayleigh–Bénard convection. *Phys. Rev.* E **63**, 045303.

ROCHE, P. E., CASTAING, B., CHABAUD, B. & HEBRAL, B. 2002 Prandtl and Rayleigh numbers dependences in Rayleigh–Bénard convection. *Europhys. Lett.* **58**, 693–698.

ROCHE, P. E., CASTAING, B., CHABAUD, B., HEBRAL, B. & SOMMERIA, J. 2001*b* Side wall effects in Rayleigh–Bénard experiments. *Eur. Phys. J.* B **24**, 405–408.

ROCHE, P.-E., GAUTHIER, F., KAISER, R. & SALORT, J. 2010 On the triggering of the ultimate regime of convection. *New J. Phys.* **12**, 085014.

SCHEEL, J. D., KIM, E. & WHITE, K. R. 2012 Thermal and viscous boundary layers in turbulent Rayleigh–Bénard convection. *J. Fluid Mech.* **711**, 281–305.

SHISHKINA, O., STEVENS, R. J. A. M., GROSSMANN, S. & LOHSE, D. 2010 Boundary layer structure in turbulent thermal convection and its consequences for the required numerical resolution. *New J. Phys.* **12**, 075022.

SHISHKINA, O. & THESS, A. 2009 Mean temperature profiles in turbulent Rayleigh–Bénard convection of water. *J. Fluid Mech.* **633**, 449–460.

STEVENS, R. J. A. M., LOHSE, D. & VERZICCO, R. 2011 Prandtl number dependence of heat transport in high Rayleigh number thermal convection. *J. Fluid Mech.* **688**, 31–43.

STEVENS, R. J. A. M., VAN DER POEL, E. P. & LOHSE, D. 2013 The unifying theory of scaling in thermal convection: The updated prefactors. *J. Fluid Mech.* **730**, 295–308.

STEVENS, R. J. A. M., VERZICCO, R. & LOHSE, D. 2010 Radial boundary layer structure and Nusselt number in Rayleigh–Bénard convection. *J. Fluid Mech.* **643**, 495–507.

SUN, C., REN, L.-Y., SONG, H. & XIA, K.-Q. 2005*a* Heat transport by turbulent Rayleigh–Bénard convection in 1m diameter cylindrical cells of widely varying aspect ratio. *J. Fluid Mech.* **542**, 165–174.

SUN, C., XI, H. D. & XIA, K. Q. 2005*b* Azimuthal symmetry, flow dynamics, and heat transport in turbulent thermal convection in a cylinder with an aspect ratio of 0.5. *Phys. Rev. Lett.* **95**, 074502.

URBAN, P., HANZELKA, P., KRALIK, T., MUSILOVA, V., SRNKA, A. & SKRBEK, L. 2012 Effect of boundary layers asymmetry on heat transfer efficiency in turbulent Rayleigh–Bénard convection at very high Rayleigh numbers. *Phys. Rev. Lett.* **109**, 154301.

URBAN, P., MUSILOVÁ, V. & SKRBEK, L. 2011 Efficiency of heat transfer in turbulent Rayleigh–Bénard convection. *Phys. Rev. Lett.* **107**, 014302.

VERZICCO, R. 2002 Sidewall finite conductivity effects in confined turbulent thermal convection. *J. Fluid Mech.* **473**, 201–210.

VERZICCO, R. & CAMUSSI, R. 1997 Transitional regimes of low-Prandtl thermal convection in a cylindrical cell. *Phys. Fluids* **9**, 1287–1295.

VERZICCO, R. & ORLANDI, P. 1996 A finite-difference scheme for three-dimensional incompressible flow in cylindrical coordinates. *J. Comput. Phys.* **123**, 402–413.

WEISS, S. & AHLERS, G. 2011 Turbulent Rayleigh–Bénard convection in a cylindrical container with aspect ratio $\Gamma = 0.50$ and Prandtl number $Pr = 4.38$. *J. Fluid Mech.* **676**, 5–40.

XI, H. D. & XIA, K. Q. 2008 Flow mode transitions in turbulent thermal convection. *Phys. Fluids* **20**, 055104.